Extraction of resonances from meson-nucleon reactions

N. Suzuki and T. Sato
Excited Baryon Analysis Center (EBAC), Thomas Jefferson National Accelerator Facility, Newport News, Virginia 23606, USA and Department of Physics, Osaka University, Toyonaka, Osaka 560-0043, Japan

T.-S. H. Lee
Excited Baryon Analysis Center (EBAC), Thomas Jefferson National Accelerator Facility, Newport News, Virginia 23606, USA and Physics Division, Argonne National Laboratory, Argonne, Illinois 60439, USA

(Received 1 July 2008; published 24 February 2009)

We present a pedagogical study of the commonly employed speed-plot (SP) and time-delay (TD) methods for extracting the resonance parameters from the data of two-particle coupled-channels reactions. Within several exactly solvable models, it is found that these two methods find poles on different Riemann sheets and are not always valid. We then develop an analytic continuation method for extracting nucleon resonances within a dynamical coupled-channel formulation of πN and γN reactions. The main focus of this paper is on resolving the complications from the coupling with the unstable $\pi\Delta$, ρN, and σN channels, which decay into $\pi\pi N$ states. By using the results from the considered exactly solvable models, explicit numerical procedures are presented and verified. As a first application of the developed analytic continuation method, we present the nucleon resonances in some partial waves extracted within a recently developed coupled-channels model of πN reactions. The results from this realistic πN model, which includes πN, ηN, $\pi\Delta$, ρN, and σN channels, also show that the simple pole parametrization of the resonant propagator using the poles extracted from SP and TD methods works poorly.

DOI: 10.1103/PhysRevC.79.025205 PACS number(s): 13.75.Gx, 13.60.Le, 14.20.Gk

I. INTRODUCTION

The excited baryon and meson states couple strongly with the continuum states. Thus they are identified with the resonance states in hadron reactions. The spectra and decay widths of the hadron resonances reveal the role of confinement and chiral symmetry of QCD in the nonperturbative region. Therefore, extraction of the basic resonance parameters from reaction data is one of the important tasks in hadron physics. Ideally, it should involve the following steps:

(i) Perform complete measurements of all independent observables of the reactions considered. For example, for pseudo-scalar meson photoproduction reactions one needs to measure eight observables [1]: differential cross sections, three single polarizations Σ, T, and P, and four double polarizations G, H, E, and F.
(ii) Extract the partial-wave amplitudes (PWA) from the data. Here we need to solve a nontrivial practical problem since all observables are bilinear combinations of PWA (i.e., $\sigma \sim f_{L'S'} f^*_{LS}$).
(iii) Extract the resonance parameters from the extracted PWA. Here the often employed methods are based on the Breit-Wigner form [2], speed-plot method of Hoehler [3,4], and time-delay method of Eisenbud [5] and Wigner [6]. A more sophisticated and rigorous method is to use the dispersion relations, K-matrix, and dynamical model to analytically continue the PWA to the complex energy plane on which the resonance poles and residues are determined. Extensive works based on these three models are reviewed in Ref. [7].

In reality, we do not have complete measurements for practically all meson-nucleon reactions. Even if the measurements are complete, step 2 requires some model assumptions to solve the inverse bilinear problem in extracting PWA. This model dependence must be taken into account in interpreting the extracted resonance parameters.

In this work, we focus on step 3 in conjunction with recent efforts in extracting the nucleon resonances from very extensive and high-quality data of meson production reactions, as reviewed in Ref. [7]. The nucleon resonances N^* and Δ listed by the Particle Data Group [8] are mainly from the analysis of πN scattering and pion photoproduction reactions. The speed-plot and time-delay methods are most often used in these analyses since they only require the PWA determined in step 2. The purpose of this work is to examine the extent to which these two methods are valid and to develop an analytic continuation method within a recently developed dynamical model [9] of meson production reactions in the nucleon resonance region.

It is useful to first briefly recall how the resonances are defined in textbooks. By analytic continuation, the scattering T-matrix can be defined on the complex energy plane. Its analytical structure is well studied [10–14] for nonrelativistic two-body scattering. For the single-channel case, the scattering T-matrix is a single-valued function of momentum p on the complex momentum p-plane, but it is a double-valued function of energy E on the complex energy E-plane because of the quadratic relation $p = |2mE|^{1/2} e^{i\phi_E/2}$. Therefore the complex E-plane is composed of two Riemann sheets. The physical (p) sheet is defined by specifying the range of phase $0 \leqslant \phi_E \leqslant 2\pi$, and the unphysical ($u$) sheet by $2\pi \leqslant \phi_E \leqslant 4\pi$. As illustrated in Fig. 1, the shaded area with $\mathrm{Im}\, p > 0$ of the upper part of Fig. 1(a) corresponds to the physical E-sheet shown in Fig. 1(b). Similarly, the unphysical E-sheet shown in Fig. 1(c) corresponds to the $\mathrm{Im}\, p < 0$ area in the lower part of Fig. 1(a).

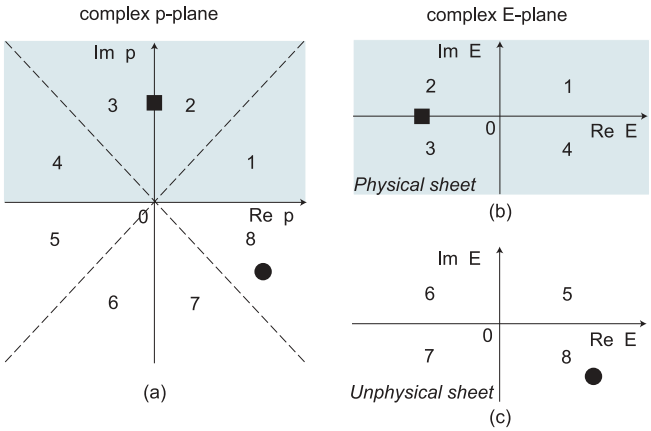

FIG. 1. (a) The complex momentum p-plane and its corresponding complex energy E-plane, which has (b) a physical sheet and (c) an unphysical sheet. Their correspondence is indicated by the same number. Solid squares (circles) represent the bound state (resonance) poles.

On the physical sheet, the only possible singularities are on the real E axis: the bound state poles [solid square in Fig. 1(b)] lie below the threshold energy $E_{\rm th}$ and the unitarity cut from $E_{\rm th}$ to infinity. On the unphysical sheet, a pole [solid circle in Fig. 1(c)] is on the lower half plane and $\mathrm{Re}E_{\rm pole} > E_{\rm th}$ corresponds to a resonance. From unitarity and analyticity of the S-matrix, each resonance pole has an accompanied pole, called a conjugate pole, that exists on the upper half of the unphysical sheet. A resonance pole corresponds to an unstable system which is formed and decays subsequently during the collision. The mathematical details of this interpretation can be found in textbooks (see, e.g., Chap. 8 of Goldberger and Watson [15]).

For the multichannel case, the analytic structure of the scattering T-matrix becomes more complex [11–14]. We postpone the discussion on this until Sec. III where a two-channel Breit-Wigner form of scattering amplitude will be used to give a pedagogical explanation.

The essential point of the time-delay and speed-plot methods is that the resonance poles just discussed can be determined from the partial-wave amplitudes defined on the physical real energies. The concept of time delay was originally introduced by Eisenbud [5] and is discussed by Wigner [6], Dalitz and Moorehouse [16], and Nussenzveig [17]. It is defined as the difference between the time in which a wave packet passes through an interaction region and the time spent by a free wave packet passing though the same distance. It was generalized to the time-delay matrix in multichannel problems and discussed further in terms of a lifetime matrix by Smith [18]. Kelkar *et al*. [19,20] applied this multichannel formulation to develop a practical time-delay method to extract hadron resonances.

The speed-plot method was developed by Hoehler [3,4] to extract the nucleon resonances from the πN partial-wave amplitudes. It is also based on the concept of time delay, but he identified resonances by "speed," which is the absolute value of the energy derivative of the scattering amplitude. The speed is always positive by its definition whereas the time delay can be negative and becomes "time advance" [21].

It is generally assumed that both the speed-plot and time-delay methods give approximate positions of the resonance poles that are rigorously defined by the analytic continuation of scattering amplitudes. However, their validity is not clear at all. Moreover, it is not clear to which Riemann sheet the pole positions extracted from using these methods belong. In this paper we analyze several exactly solvable models to clarify these questions. In particular, we find that these two methods give poles on different Riemann sheets.

We then develop an analytic continuation method for extracting the resonance parameters within a recently developed Hamiltonian formulation [9] of meson-nucleon reactions. We first establish the method by using several exactly solvable models. The main task here is to handle the singularities associated with the unstable particle channels such as $\pi\Delta$, ρN, and σN. We then apply the method to extract the nucleon resonances in some partial waves of πN scattering within the dynamical coupled-channels model developed in Ref. [22]. The analytical structure of the resonance propagator is also analyzed within this model.

In Sec. II, we describe the formula for applying the speed-plot and time-delay methods. These two methods are then analyzed and tested in Sec. III by using the commonly used two-channel Breit-Wigner form of the S-matrix. In Sec. IV, we develop an analytic continuation method by using several exactly solvable resonance models and further test the speed-plot and time-delay methods. Section V is devoted to resolving the complications from couplings with unstable particle channels. In Sec. VI, we present the results from applying the developed analytic continuation method to extracting nucleon resonances in some partial waves within the πN model of Ref. [22]. A summary is given in Sec. VII.

II. FORMULA FOR TIME-DELAY AND SPEED-PLOT METHODS

The objective of the time-delay (TD) and speed-plot (SP) methods is to determine the mass M_R and width Γ_R of a resonance from the S-matrix of reactions. In this section, we will not explain how these two methods were introduced, as briefly discussed in Sec. I. Rather, we only give their formula in practical applications.

For the single-channel elastic scattering case, the time delay of the outgoing wave packet with respect to the noninteracting wave packet in a given partial wave is defined [6,16,17] as

$$\Delta t(E) = \mathrm{Re}\left(-i\frac{1}{S(E)}\frac{dS(E)}{dE}\right), \tag{1}$$

where the S-matrix is related to the phase shift δ by

$$S(E) = e^{2i\delta}. \tag{2}$$

Equations (1) and (2) lead to the following simple expression of time delay:

$$\Delta t = 2\frac{d\delta}{dE}. \tag{3}$$

The TD method aims at finding the resonance mass M_R by finding the maximum of the time delay,

$$\left.\frac{d\Delta t}{dE}\right|_{E=M_R} = 0. \tag{4}$$

As an ideal example, we evaluate the time delay for the S-matrix defined by the well-known Breit-Wigner resonance formula

$$S(E) = \frac{E - M_R - i\Gamma_R/2}{E - M_R + i\Gamma_R/2}. \tag{5}$$

Equation (1) then leads to

$$\Delta t = \frac{\Gamma_R}{(E - M_R)^2 + \Gamma_R^2/4}, \tag{6}$$

which obviously takes a maximum at $E = M_R$ and hence M_R is defined as the resonance mass. It also gives the following simple physical interpretation of the width Γ_R in terms of the time delay of the wave packet passing through the interaction region:

$$\Delta t|_{E=M_R} = \frac{4}{\Gamma_R}. \tag{7}$$

Here and in the rest of this paper, the normalization is chosen such that the S-matrix is related to the T-matrix by

$$S(E) = 1 + 2iT(E). \tag{8}$$

We then note that, for the S-matrix in Eq. (5), the width can also be expressed in terms of the T-matrix as

$$\frac{\Gamma_R}{2} = \left[\frac{|T|}{|\frac{dT}{dE}|}\right]_{E=M_R}. \tag{9}$$

In the analysis of πN scattering, Hoehler [3,4] introduced the SP method. The speed is defined as

$$\mathrm{sp}(E) = \left|\frac{dT}{dE}\right|. \tag{10}$$

By using Eqs. (2) and (3), Eq. (10) leads to

$$\mathrm{sp}(E) = \frac{|\Delta t|}{2}. \tag{11}$$

Thus the speed is also related to the time delay of the wave packet. The SP method defines the resonance mass M_R by the maximum of the speed,

$$\frac{d}{dE}\mathrm{sp}(E)\,|_{E=M_R} = 0. \tag{12}$$

From Eqs. (4), (11), and (12), it is obvious that the speed plot and time delay will give the same resonance mass for the single-channel elastic scattering case.

For multichannel reactions with N open channels, the S-matrix becomes an $N \times N$ matrix $\hat{S}(E)$. Smith [18] introduced a lifetime matrix $\hat{Q}$ defined by

$$\hat{Q}(E) = -i\,\hat{S}(E)^{\dagger}\frac{d\hat{S}(E)}{dE}. \tag{13}$$

This equation can be considered as an extension of Eq. (1) of the single-channel case. The trace of the lifetime matrix can be expressed in terms of eigenphases δ_i of the S-matrix [23–25],

$$\mathrm{Tr}\hat{Q}(E) = 2\frac{d(\sum_i \delta_i)}{dE}. \tag{14}$$

The resonance mass M_R is then obtained by finding

$$\left.\frac{d\mathrm{Tr}\hat{Q}(E)}{dE}\right|_{E=M_R} = 0. \tag{15}$$

However, the eigenphases δ_i can be obtained only when we know all of the S-matrix elements associated with all open channels. In practice, only the elastic scattering amplitude and a few of the inelastic amplitudes can be extracted from the data. Therefore Eqs. (14) and (15) of Smith's TD method cannot be used rigorously in practice.

Here we focus on the TD method used by Kelkar and coworkers [19–21]. They defined the time delay td for the channel i only by the diagonal component S_{ii} of the S-matrix and its derivative,

$$\mathrm{td}(E) = \mathrm{Re}\left(-i\frac{1}{S_{ii}}\frac{dS_{ii}}{dE}\right). \tag{16}$$

Obviously, this method is identical to Eq. (1) of the single-channel case except that the S-matrix element here is $S_{ii} = \eta e^{2i\delta}$ with η denoting the inelasticity. Equation (16) can be considered as an approximation of Eq. (13) by neglecting the inelastic channels in summing the intermediate states. In Refs. [19–21], the resonance mass M_R is determined by the maximum of the time delay,

$$\frac{d}{dE}\mathrm{td}(E)\,|_{E=M_R} = 0, \tag{17}$$

and the width Γ_R by

$$\mathrm{td}(M_R \pm \Gamma_R/2) = \mathrm{td}(M_R)/2. \tag{18}$$

The SP method for the multichannel case involves simply defining the speed sp by the diagonal T_{ii} of the T-matrix,

$$\mathrm{sp}(E) = \left|\frac{dT_{ii}}{dE}\right|, \tag{19}$$

and defining [3] the width Γ_R by assuming that the T-matrix element can be parametrized as

$$T_{ii}(E) = T_b(E) + z(E)\frac{\Gamma_R/2}{E - M_R + i\Gamma_R/2}. \tag{20}$$

Here T_b is an nonresonant amplitude and the resonant amplitude is defined by the resonance mass M_R, the width Γ_R, and a complex residue $z(W)$. By assuming that the energy dependence of $T_b(W)$, $z(W)$, and Γ_R can be neglected at energies near M_R, Eqs. (19) and (20) obviously satisfy Eq. (12) and lead to the following condition:

$$\mathrm{sp}(M_R \pm \Gamma_R/2) = \mathrm{sp}(M_R)/2. \tag{21}$$

Equations (19), (12), and (21) are used in applying the SP method to extract the resonance mass M_R and width Γ_R from the partial-wave amplitudes. Equation (20) is not needed in practice, but it is an essential assumption of the SP method.

III. ANALYSIS OF SPEED-PLOT AND TIME-DELAY METHODS

To examine the SP and TD methods, we consider a commonly used two-channel Breit-Wigner (BW) amplitude, which can be derived [11,14,26,27] from the analytical property of the S-matrix. To make contact with what we will discuss in the rest of this paper, we will indicate here how this amplitude can be derived from a Hamiltonian formulation of meson-baryon reactions, such as that developed in Ref. [9].

It is sufficient to consider the simplest two-channel case with a nonrelativistic two-particle Hamiltonian defined by

$$H = H_0 + V. \tag{22}$$

In the center-of-mass frame H_0 can be written as

$$H_0 = \sum_i |i\rangle \left[m_{i1} + m_{i2} + \frac{p^2}{2\mu_i} \right] \langle i|, \tag{23}$$

where m_{ik} is the mass of kth particle in channel i, and $\mu_i = m_{i1}m_{i2}/(m_{i1} + m_{i2})$ is the reduced mass. In each partial wave, the S-matrix is a 2×2 matrix and can be written as

$$S = \frac{1 - i\pi\rho K}{1 + i\pi\rho K}, \tag{24}$$

where ρ is the density of state and the K-matrix, which is also a 2×2 matrix, is defined by the following Lippmann-Schwinger equation:

$$K(E) = V + V \frac{P}{E - H_0} K(E). \tag{25}$$

Here P means taking the principal value of the integration over the propagator.

We now consider the on-shell matrix element of the S-matrix of Eq. (24). If the on-shell momentum is denoted as p_i for channel i, we then have

$$\langle i|1 \pm i\pi\rho K|j\rangle = \delta_{i,j} \pm i\pi\rho_i K_{i,j}, \tag{26}$$

where $\rho_i = p_i\mu_i$. The S-matrix element of $1 \to 1$ elastic scattering is then of the following explicit form:

$$S_{11} = \frac{(1 - i\pi\rho_1 K_{11})(1 + i\pi\rho_2 K_{22}) - \pi^2\rho_1\rho_2 K_{12}K_{21}}{(1 + i\pi\rho_1 K_{11})(1 + i\pi\rho_2 K_{22}) - \pi^2\rho_1\rho_2 K_{11}K_{22}}. \tag{27}$$

If we assume that at energies near the resonance energy the K-matrix can be approximated as

$$K_{ij} \sim \frac{g_i g_j}{E - M}, \tag{28}$$

where M is a real-valued mass parameter, Eq. (27) can then be written as

$$S_{11} = \frac{E - M - ip_1\gamma_1 + ip_2\gamma_2}{E - M + ip_1\gamma_1 + ip_2\gamma_2}. \tag{29}$$

Here we have defined $\gamma_i = \pi g_i^2 \mu_i > 0$. If we further assume that γ_i is independent of scattering energy, Eq. (29) is the commonly used two-channel BW formula [26–28]. In the rest of this section, we will follow these earlier works and treat γ_1 and γ_2 as energy-independent parameters of the model.

Since the scattering T-matrix is related to the S-matrix by

$$S_{11}(E) = 1 + 2iT_{11}(E), \tag{30}$$

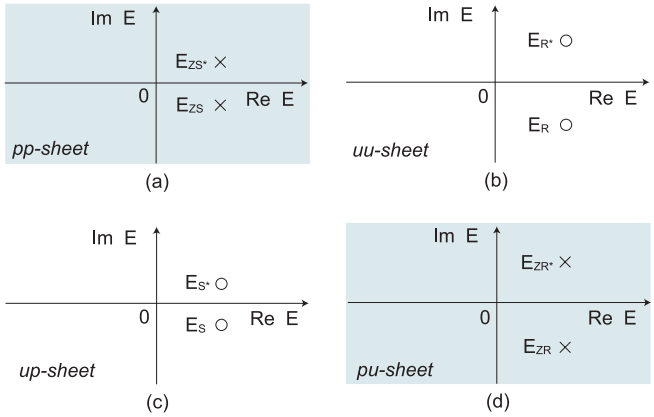

FIG. 2. Poles and zeros of the simplified two-channel Breit-Wigner form ($\mu_1 = \mu_2$ and $\Delta = 0$) of the S-matrix on the complex E-plane, which has pp, uu, up, and pu sheets. The open circles on the uu-sheet (b) are the resonance pole E_R and its conjugate pole E_R^*. The open circles on the up-sheet (c) are the shadow pole E_S and its conjugate pole E_S^*. The crosses on the pp-sheet (a) are the zero E_{ZS} and its conjugate E_{ZS}^*, which are at the same energies of the shadow poles E_S and E_S^*. The crosses on the pu-sheet (d) are the zero E_{ZR} and its conjugate E_{ZR}^*, which are at the same energies of the resonance poles E_R and E_R^*.

Eq. (29) leads to

$$T(E) = T_{11}(E) = \frac{-\gamma_1 p_1}{E - M + i\gamma_1 p_1 + i\gamma_2 p_2}. \tag{31}$$

From now on we use the notation $T(E)$ for the $1 \to 1$ amplitude $T_{11}(E)$.

A. Analytic Properties of the S-matrix

Within the two-channel BW model specified here, we will analyze in this section the analytic properties of the S-matrix on the complex energy E-plane. This will also allow us to explain clearly some terminology that is commonly seen but often not explicitly explained in the literatures on resonance extractions.

The on-shell momenta p_i for channel i is defined by

$$E_i = \frac{p_i^2}{2\mu_i}, \tag{32}$$

where

$$E_i = E - (m_{i1} + m_{i2}). \tag{33}$$

We can define the threshold variable Δ between two channels by

$$E_1 = \frac{p_2^2}{2\mu_2} + \frac{\Delta^2}{2\mu_1}, \tag{34}$$

where

$$\frac{\Delta^2}{2\mu_1} = m_{21} + m_{22} - m_{11} - m_{12} \tag{35}$$

is the threshold energy of the second channel.

The momenta at poles of the S-matrix in Eq. (29) can be determined by solving

$$E - M + ip_1\gamma_1 + ip_2\gamma_2 = 0. \tag{36}$$

By using Eqs. (32)–(35), this equation can be written as

$$p_1^4 + ap_1^3 + bp_1^2 + cp_1 + d = 0, \tag{37}$$

where

$$a = i4\mu_1\gamma_1, \tag{38}$$
$$b = 4\mu_1\left(\mu_2\gamma_2^2 - M - \mu_1\gamma_1^2\right), \tag{39}$$
$$c = -8i\mu_1^2 M\gamma_1, \tag{40}$$
$$d = 4\left(\mu_1^2 M^2 - \mu_1\mu_2\gamma_2^2\Delta^2\right). \tag{41}$$

Equation (37) means that the BW amplitude of Eq. (29) has four poles. Each pole is specified by two on-shell momenta $P_\alpha = (p_{1\alpha}, p_{2\alpha})$ with $\alpha = 1, 2, 3, 4$. The analytic properties of the S-matrix of Eq. (29) depends on how these poles are located on the complex energy E-plane. As we explained in Sec. I, the energy plane for each channel has two Riemann sheets because of the quadratic relation [Eq. (32)] between the momentum p_i and energy E_i; namely, $p_i = \sqrt{2\mu_i|E_i|}e^{i\phi_i/2}$ for $i = 1, 2$. For each channel, the physical (p) sheet is defined by specifying the range of phase $0 \leqslant \phi_i \leqslant 2\pi$, and the unphysical ($u$) sheet by $2\pi \leqslant \phi_i \leqslant 4\pi$. The correspondence between the momentum p_i-plane and the energy E_i-plane is similar to that illustrated in Fig. 1. For the considered two-channel case, we thus have four energy sheets specified by the signs of $\mathrm{Im}p_1$ and $\mathrm{Im}p_2$: pp, up, uu, and pu, as shown in Fig. 2. Thus each of four poles $P_\alpha = (p_{1\alpha}, p_{2\alpha})$ can be on one of these E-sheets.

To be more specific, we now consider the case that is most relevant to our study of nucleon resonances, that is, the $\mathrm{Re}E_1 > 0$ and $\mathrm{Re}E_2 > 0$ case for which the poles are all above the thresholds of both channels. From Eq. (36), we immediately notice that if (p_{1a}, p_{2a}) with $E = E_a$ is one of the solutions, $(-p_{1a}^*, -p_{2a}^*)$ with $E = E_a^*$ is also a solution. Therefore the four poles determined by Eq. (37) can be grouped into two pairs. In the following discussion, they are denoted as (E_a, E_a^*) and (E_b, E_b^*). Without losing generality, one can assume that one of the poles is in the range of $(\mathrm{Re}p_1 > 0, \mathrm{Re}p_2 > 0)$ and the other in the range of $(\mathrm{Re}p_1 < 0, \mathrm{Re}p_2 < 0)$. If the first pole (p_{1a}, p_{2a}) is in the region where $(\mathrm{Re}p_{1a} > 0, \mathrm{Re}p_{2a} > 0)$ and $(\mathrm{Im}p_{1a} < 0, \mathrm{Im}p_{2a} < 0)$; it is a pole, denoted as E_R, on the uu-sheet of Fig. 2. This pole is usually called the resonance pole and is closer than other poles on up- or pu-sheets to the physical pp-sheet, as will be explained later. In the Hamiltonian formulation considered in this work and in the well-developed collision theory, a resonance pole can be mathematically derived [15] from the mechanism that an unstable system is formed and decays subsequently during the collision. The resonance pole E_R has an accompanied pole E_R^* at $(-p_{1a}^*, -p_{2a}^*)$ that is also on the uu-sheet, as shown in Fig. 2. E_R^* is called the "conjugate pole" of E_R.

The second pole at (p_{1b}, p_{2b}) with $\mathrm{Im}p_{1b} < 0$ and $\mathrm{Im}p_{2b} > 0$ ($\mathrm{Im}p_{1b} > 0$ and $\mathrm{Im}p_{2b} < 0$) may be on the up-sheet (pu-sheet), depending on the parameters γ_1 and γ_2. This pole is called the shadow pole [29]. A shadow pole on the up-sheet and its conjugate pole are E_S and E_S^* in Fig. 2.

We now note that in this simple BW model, the zeros of the S-matrix of Eq. (29), where $S_{11}(E) = 0$, is defined by its numerator

$$E - M - ip_1\gamma_1 + ip_2\gamma_2 = 0. \tag{42}$$

This equation can be cast into the form of Eq. (36) by simply replacing p_1 by $-p_1$. Thus solutions of Eq. (42), called the zeros of the S-matrix, can be readily obtained from the solutions (p_{1a}, p_{2a}) and (p_{1b}, p_{2b}) of Eq. (36). They are $(-p_{1\alpha}, p_{2\alpha})$ with E_α and $(p_{1\alpha}^*, -p_{2\alpha}^*)$ with E_α^* for $\alpha = a, b$. The zero at $(-p_{1b}, p_{2b})$ is on the pp-sheet, denoted as E_{ZS} and E_{ZS}^* in Fig. 2. Similarly, the zero at $(-p_{1a}, p_{2a})$ is on the pu-sheet, shown as E_{ZR} together with its conjugate E_{ZR}^* in Fig. 2. Note that Fig. 2 is for the case that the parameters γ_1 and γ_2 are chosen such that the shadow poles E_S and its conjugate E_S^* are on the up-sheet. For other possible γ_1 and γ_2, the pole positions could be different from what are shown in Fig. 2, but their close relations, as just discussed, are the same.

From this analysis, it is clear that the poles and zeros of the S-matrix are closely related. Their locations on the four Riemann sheets can be conveniently displayed on one complex plane by introducing a variable t [30] such that

$$p_1 = \Delta\frac{1+t^2}{1-t^2}, \tag{43}$$
$$p_2 = 2\Delta\sqrt{\frac{\mu_2}{\mu_1}}\frac{t}{1-t^2}. \tag{44}$$

Hence each point in the t-plane corresponds to a set of (p_1, p_2). In Fig. 3, the resonance position E_R and shadow E_S poles and their conjugate poles and zeros of the S-matrix, E_{ZS}, E_{ZR}, E_{ZS}^*, and E_{ZR}^*, are shown on the t-plane. The physical S-matrix at real energies, which determine the observables, are on the bold lines. The zero energy and the threshold of the second channel correspond to $t = i$ and $t = 0$, respectively. One can see that the resonance pole E_R is closer than the shadow pole E_S to the bold lines (S-matrix) and hence can have the largest effect on the observables. Consequently, most of the rapid energy

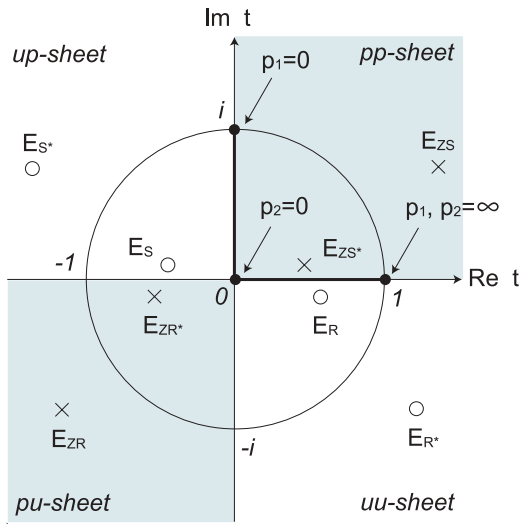

FIG. 3. The poles and zeros of the S-matrix shown in Fig. 2 displayed on the complex t-plane defined by Eqs. (43) and (44).

dependence of observables is attributed to the resonance poles, not the shadow poles or the other poles shown in Fig. 3. However, the zero E^*_{ZS} of the S-matrix is also close to the bold lines. As seen in the derivations just given, this zero E^*_{ZS} is closely related to shadow pole E_S. Thus the shadow poles can also be related to the observables. Of course, which pole is most important in determining the rapid energy dependence of observables also depends on the residues of the T-matrix at the pole positions.

In the next section, we will use a further simplified BW form to explain more clearly the close relations between the poles and zeros of the S-matrix. In particular, we will see explicitly that the shadow pole E_S in Fig. 2, which is not on the same Riemann sheet as E_R, can be located by the zeros of the S-matrix. More importantly, we will also see how the SP and TD methods work both analytically and numerically.

B. Positions of poles

For simplicity, we assume that the threshold energies of the two channels are the same and hence $\mu \equiv \mu_1 = \mu_2$ and $\Delta = 0$. Therefore we have simple relations between energy and momenta: $E = p_1^2/2\mu = p_2^2/2\mu$ and $p \equiv p_1 = \pm p_2$. As discussed in the previous section, the four Riemann sheets are classified by the sign of the imaginary part of the momentum; namely, the physical (unphysical) sheet is assigned by $\mathrm{Im}p > 0\,(\mathrm{Im}p < 0)$. With the simplification $p \equiv p_1 = \pm p_2$, we obviously have $p_1 = p_2 = p$ on the pp- and uu-sheets and $p_1 = -p_2 = p$ on up- and pu-sheets.

Let us start with the case of $p_1 = p_2 = p$ for the pp-sheet or uu-sheet. The S-matrix element of Eq. (29) of the first channel can be written as

$$S_{11}(E) = \frac{E - M - i(\gamma_1 - \gamma_2)p}{E - M + i(\gamma_1 + \gamma_2)p}. \tag{45}$$

It can be recast into the following more transparent form:

$$S_{11}(E) = \frac{(p + p_S)(p - p_S^*)}{(p - p_R)(p + p_R^*)}, \tag{46}$$

with

$$p_R = \sqrt{2\mu M - (\mu\gamma_+)^2} - i\mu\gamma_+, \tag{47}$$

$$p_S = \sqrt{2\mu M - (\mu\gamma_-)^2} - i\mu\gamma_-, \tag{48}$$

where

$$\gamma_\pm = \gamma_1 \pm \gamma_2, \tag{49}$$

remembering that we consider $\gamma_1 > 0$ and $\gamma_2 > 0$. To make use of Fig. 2 in the following discussion, we consider the case that $\gamma_1 > \gamma_2$ and hence $\gamma_\pm > 0$ and both p_R and p_S defined in Eqs. (47) and (48) are associated with the unphysical u-sheet. For the case of $\gamma_- < 0$, p_S is associated with the physical p-sheet and the following presentation can be easily modified to account for this case.

Clearly, Eq. (46) means that the S-matrix has a pole at $p_1 = p_2 = p = p_R$ on the uu-sheet with a resonance energy

$$E_R = \frac{p_R^2}{2\mu} = M - \mu\gamma_+^2 - i\gamma_+\sqrt{\mu(2M - \mu\gamma_+^2)}. \tag{50}$$

Its conjugate pole E_R^* is at $p_1 = p_2 = p = -p_R^*$. The positions of E_R and E_R^* are shown in the upper right side of Fig. 2. Equation (46) also indicates that the zero of the S-matrix is at $p_1 = p_2 = -p_S$, which is on the pp-sheet because of $\mathrm{Im}(-p_S) > 0$. The energy of this zero of the S-matrix is

$$E_{ZS} = \frac{p_S^2}{2\mu} = M - \mu\gamma_-^2 - i\gamma_-\sqrt{\mu(2M - \mu\gamma_-^2)}. \tag{51}$$

Its conjugate E^*_{ZS} is at $p_1 = p_2 = p_S^*$. The positions of E_{ZS} and E^*_{ZS} are on the pp-sheet, as shown in the upper left side of Fig. 2.

We next consider the $p_1 = -p_2 = p$ case that the poles and zeros of the S-matrix are on the up- or pu-sheets. The S-matrix of Eq. (29) for this case then takes the following form:

$$S_{11}(E) = \frac{E - M - i(\gamma_1 + \gamma_2)p}{E - M + i(\gamma_1 - \gamma_2)p}. \tag{52}$$

By comparing Eq. (45) and Eq. (52) and using the variables p_R and p_S defined by Eqs. (47) and (48), Eq. (52) can be written as

$$S_{11}(E) = \frac{(p + p_R)(p - p_R^*)}{(p - p_S)(p + p_S^*)}. \tag{53}$$

This equation indicates that, for the considered $\gamma_- > 0$, the S-matrix has a shadow pole at $p_1 = -p_2 = p = p_S$ on the up-sheet. Thus its position $E_S = p_S^2/(2\mu)$ is identical to E_{ZS} of the zero of the S-matrix on the pp-sheet; namely,

$$\begin{aligned} E_S &= E_{ZS} \\ &= \frac{p_S^2}{2\mu} = M - \mu\gamma_-^2 - i\gamma_-\sqrt{\mu(2M - \mu\gamma_-^2)}. \end{aligned} \tag{54}$$

This means that the shadow pole E_S on the up-sheet can be found from searching for the zero E_{ZS} of the S-matrix on the pp-sheet.

Equation (53) also gives a zero of the S-matrix at $p_1 = -p_2 = p = -p_R$ on the pu-plane because $\mathrm{Im}(-p_R) > 0$. Its energy E_{ZR} is also identical to the E_R value defined earlier:

$$\begin{aligned} E_{ZR} &= E_R \\ &= \frac{p_R^2}{2\mu} = M - \mu\gamma_+^2 - i\gamma_+\sqrt{\mu(2M - \mu\gamma_+^2)}. \end{aligned} \tag{55}$$

The positions of E_S and E_{ZR} and their conjugates E_S^* and E^*_{ZR} are also in the lower parts of Fig. 2.

From this analysis for the $\gamma_- > 0$ case, we see that the energies of the resonance poles may be obtained by studying the poles of the S-matrix on the uu-sheet and those of the shadow poles may be obtained from the zeros of the S-matrix on the pp-sheet. The analysis for the $\gamma_- < 0$ case is similar. Here we only mention that when $\gamma_- > 0$ is changed to $\gamma_- < 0$, the shadow poles E_S and E_S^* on the up-sheet move to the pu-sheet and zeros E_{ZS} and E^*_{ZS} will be on the uu-sheet.

Now let us examine how the SP and TD methods can be used to find the poles defined by these exact expressions of the two-channel BW amplitude. We first recall that in applying the SP and TD methods, the energy E and momentum p_i in the S-matrix are restricted on the positive real axis. For the considered simplified case, we thus have $p_1 = p_2 = p$ and

the T-matrix of Eq. (31) then becomes

$$T(E) = \frac{-\gamma_1 p}{E - M + i\gamma_+ p}. \tag{56}$$

Our task is to examine whether the resonance mass M_R and width Γ_R found by applying the SP and TD methods on Eq. (56) are close to the real and imaginary parts of the poles defined in the previous section.

According to Eqs. (12) and (19), the SP method finds the resonance mass M_R by finding the maximum of the speed through the use of the condition

$$\left[\frac{d}{dE}\left|\frac{dT}{dE}\right|\right]_{E=M_R} = 0. \tag{57}$$

With the T-matrix from Eq. (56), Eq. (57) leads to the following equation:

$$3M_R^3 + (3M + 2\mu\gamma_+^2)M_R^2 - (7M^2 - 6\mu M\gamma_+^2)M_R + M^3 = 0. \tag{58}$$

This equation can be written in the dimensionless form as

$$3\tilde{E}^3 + (3 + 2\alpha)\tilde{E}^2 - (7 - 6\alpha)\tilde{E} + 1 = 0, \tag{59}$$

with $\tilde{E} = M_R/M$ and $\alpha = \mu\gamma_+^2/M_R$. By inspection, one can see that Eq. (59) has real and positive M_R solutions only in the $\alpha < 0.417$ region. Two of the three solutions are the maximum and minimum points of the speed, and the third one is less than 0. The SP method defines the maximum point of the speed as the resonance mass. We find that this solution can be expanded as

$$[M_R]_{\rm SP} = M - \mu\gamma_+^2 - \frac{1}{4M}(\mu\gamma_+^2)^2 + O\left(\frac{(\mu\gamma_+^2)^3}{M^2}\right). \tag{60}$$

Clearly, $[M_R]_{\rm SP}$ equals to the real part of Eq. (50) if we neglect the second- and higher order terms in the expansion in powers of $\mu\gamma_+^2/M$. Therefore the SP method is accurate only under the condition that $\mu\gamma_+^2/M \ll 1$. Moreover, it is clear from this equation that speed has no stationary point for $\mu\gamma_+^2/M > 0.417$ and therefore the SP method will fail to find the pole even if there is a pole within the model.

We next turn to discussing the width Γ_R obtained by the SP method. It is evaluated by using Eq. (9). We find that it can also be expanded as

$$\frac{[\Gamma_R]_{\rm SP}}{2} \equiv \frac{|T|_{[M_R]_{\rm SP}}}{\left|\frac{dT}{dE}\right|_{[M_R]_{\rm SP}}} = \sqrt{\mu\gamma_+^2(2M - \mu\gamma_+^2)} \times \left[1 - \frac{\mu\gamma_+^2}{2M} + O\left(\left(\frac{\mu\gamma_+^2}{M}\right)^2\right)\right]. \tag{61}$$

Here again, if we neglect higher order terms of $\mu\gamma_+^2/M$, the SP method can give the imaginary part of E_R of the exact expression [Eq. (50)]. As we have seen in Fig. 2, the two-channel BW S-matrix has two pairs of poles on the uu-sheet and the up-sheet. However, the SP method can only find the pole E_R on the uu-sheet.

From this analysis, it is clear that the accuracy of the SP method is controlled by $\mu\gamma_+^2/M$. We examine this by using an example with $\mu = \frac{m_N m_\pi}{m_N + m_\pi}$, where $m_N = 938.5$ MeV and $m_\pi = 139.6$ MeV, and $M = m_N + m_\pi + 600$ MeV. In Fig. 4 the solid curves are the pole positions on the uu-sheet. They are obtained from evaluating the exact analytical formula [Eq. (50)] for $\gamma_-/\gamma_+ = 0.5$ and varying $\mu\gamma_+^2/M$ from 0.01 to 0.6. With the same parameters we then apply the SP method to search for the pole $(M_R, -i\Gamma_R/2)$ from the amplitude [Eq. (56)] numerically by using Eqs. (9), (10), and (12). The obtained pole positions are the filled squares shown in Fig. 4. As expected, the SP method works very well for small $\mu\gamma_+^2/M$. However, the pole position from the SP method starts to deviate from the exact results (solid curves) as $\mu\gamma_+^2/M$ increases. There are no filled squares in Fig. 4 in the region $\mu\gamma_+^2/M > 0.417$ because the SP method cannot find a pole in this region. This is not because of the numerical accuracy of our calculation, but it is, as mentioned, the intrinsic limitation of the SP method.

We now turn to investigating the TD method. We apply Eq. (17) to search for the resonance mass M_R from the amplitude [Eq. (56)]. Since it is not clear how to interpret Kelkar's prescription [Eq. (18)], we assume that the S-matrix

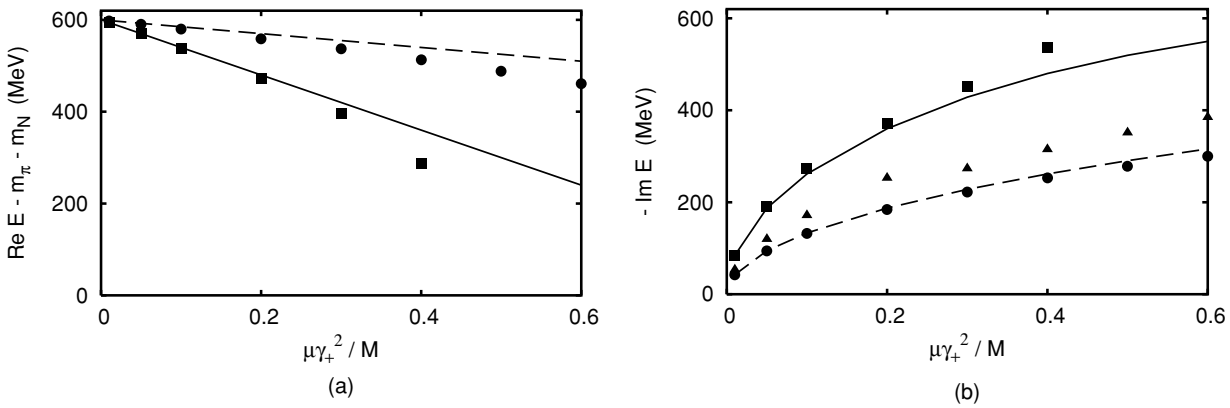

FIG. 4. The $\mu\gamma_+^2/M$ dependence of the pole positions on the uu-sheet (solid curve) and up-sheet (dashed curve) of the simplified two-channel Breit-Wigner form ($\mu_1 = \mu_2$, $\Delta = 0$) calculated at $\gamma_-/\gamma_+ = 0.5$. The real and imaginary parts of poles are shown in panels (a) and (b), respectively. The solid squares (solid circles) are the results obtained from using the SP (TD) method. Triangles in (b) are the widths of the poles obtained using Eq. (18).

element S_{11} is of the following form:

$$S_{11}(E) = \frac{E - M - i\Gamma_S/2}{E - M + i\Gamma_R/2} \tag{62}$$

$$= \eta e^{2i\delta}. \tag{63}$$

Then Eq. (18) leads to an improved expression for the width Γ_S:

$$\frac{[\Gamma_R]_{\rm TD}}{2} = \frac{\Gamma_S}{2} \equiv \frac{1 \pm \eta}{2} \left| \frac{1}{\frac{d\delta}{dE}} \right|_{E=[M_R]_{\rm TD}}, \tag{64}$$

where $+$ $(-)$ of $\pm$ is for the maximum (minimum) of the TD, suggesting the pole on the up- (pu-) sheet. We have found that the TD method, defined by Eq. (17) and Eq. (64), can only find the shadow poles on the up-sheet that are given by the exact expression, Eq. (54). The results from using the same parameters specified here are also shown in Fig. 4. The dashed curves are from the exact expression, Eq. (54), and the solid dots are from applying Eq. (17) and Eq. (64) to search numerically for the poles from Eq. (52). Clearly, the TD method works very well in finding the shadow poles on the up-sheet. In the same figure the triangles are from using Kelkar's prescription [Eq. (18)]. Obviously, our formula [Eq. (64)] works better. We have also examined the TD for $\gamma_- < 0$. In this case the TD becomes negative and has a minimum. We apply Eq. (17) for the minimum of the TD and find that TD method also works well in finding the pole on the pu-sheet.

IV. ANALYTIC CONTINUATION OF RESONANCE MODELS

With the analysis presented in the previous section, it is clear that the empirical partial-wave amplitudes determined from experimental data cannot be blindly used to extract resonance parameters by using SP or TD methods. To make progress, one needs to construct a reaction model to fit the data and then extract the resonance parameters by analytic continuation within the model. In this paper, we focus on a dynamical model [9] that accounts for the main features of meson production reactions in the nucleon resonance region. Our task in this section is to develop numerical methods for finding the resonance poles from such models that do not have analytical forms of their solutions. We will first consider the simplest one-channel and one-resonance case, then two-channel and one-resonance and finally two-channel and two-resonance cases. All of these models are exactly solvable such that their poles are known analytically and the developed numerical methods can be tested.

A. One-channel, one-resonance case

To be specific, we consider the two-particle reactions defined by the following well-known isobar Hamiltonian in the center-of-mass frame:

$$H = H_0 + H', \tag{65}$$

with

$$H_0 = [E_1(\vec{p}) + E_2(-\vec{p})] + |N_0\rangle M_0 \langle N_0|, \tag{66}$$

$$H' = |g\rangle\langle g|, \tag{67}$$

where M_0 is the mass parameter of a bare particle N_0, which can decay into two particle states through the vertex interaction g in H', and $E_i(p) = [m_i^2 + p^2]^{1/2}$ is the energy of the ith particle. The scattering operator is defined by

$$t(E) = H' + H' \frac{1}{E - H_0 - H'} H', \tag{68}$$

which leads to the following Lippmann-Schwinger equation for the scattering amplitudes in each partial wave:

$$t(p', p; E) = v(p', p; E) + \int_{C_0} dq\, q^2 \frac{v(p', q; E) t(q, p; E)}{E - E_1(q) - E_2(q)}, \tag{69}$$

where the integration path C_0 will be specified later. The interaction in Eq. (69) is

$$v(p', p; E) = \frac{g(p')g(p)}{E - M_0}. \tag{70}$$

Equations (69) and (70) lead to the following well-known solution:

$$t(p', p; E) = \frac{g(p')g(p)}{E - M_0 - \Sigma(E)}, \tag{71}$$

with

$$\Sigma(E) = \int_{C_0} dp\, p^2 \frac{g^2(p)}{E - E_1(p) - E_2(p)}. \tag{72}$$

From the analysis in the previous section, the resonance poles can be found from $t(E) = t(p_0, p_0; E)$ on the unphysical Riemann sheet defined by ${\rm Im} p_0 < 0$ with p_0 denoting the on-shell momentum,

$$E = \sqrt{m_1^2 + p_0^2} + \sqrt{m_2^2 + p_0^2}. \tag{73}$$

Obviously, p_0 is also the pole position of the propagator in Eq. (69) or Eq. (72).

The physical scattering amplitude at a positive energy E can be obtained from Eq. (69) or Eq. (71) by setting $E \to E + i\epsilon$ with a positive $\epsilon \to 0$ and choosing the integration contour C_0 to be along the real axis of p with $0 \leqslant p \leqslant \infty$. From Eq. (69) it is clear that $t(E)$ has a discontinuity on the positive real E,

$$\begin{aligned} {\rm Dis}[t(E)] &= t(E + i\epsilon) - t(E - i\epsilon) \\ &= 2\pi i \rho(p_0) v(p_0, p_0) t(E), \end{aligned} \tag{74}$$

where $\rho(p_0) = p_0 E_1(p_0) E_2(p_0)/E$. Thus the t-matrix has a cut running along the real positive E. To find resonance poles, we need to find the solution of Eq. (69) on the unphysical sheet with ${\rm Im} p \leqslant 0$ on which the pole p_0 of the propagator moves into the lower p-plane, as shown in Fig. 5(a). From Eq. (74), it is clear that the solution of Eq. (69), with the contour C_0 chosen to be on the real axis $0 \leqslant p \leqslant \infty$, will encounter the discontinuity and is not the solution on the unphysical sheet where we want to search for the resonance poles. It is well known [28,31–33] that this difficulty can be overcome

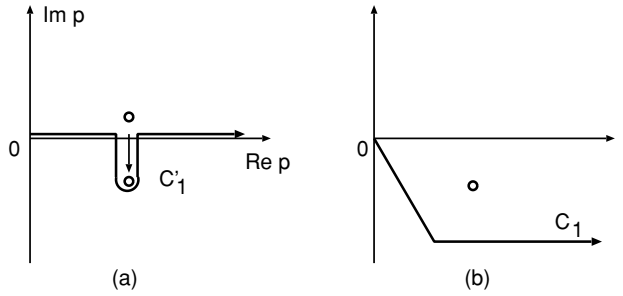

FIG. 5. The shift of the singularity (open circle) of the propagator of the two-particle scattering equation [Eq. (69)] as energy E moves from the physical sheet to the unphysical sheet. C_1' in (a) or C_1 in (b) is the integration path for calculating the scattering amplitude with E on the unphysical plane.

by deforming the integration path to the contour C_1' shown in Fig. 5(a). In this way the pole will not cross the cut and the integral is analytically continued from real positive E to the lower half of the unphysical E-sheet with $\mathrm{Im}\, p_0 \leqslant 0$. Obviously, the same solution can be obtained by choosing any contour that is below the pole position p_0, such as the contour C_1 of Fig. 5(b).

With the solution of the form of Eq. (71), the numerical procedure of finding resonance poles is to solve

$$E - M_0 - \Sigma(E) = 0, \tag{75}$$

with

$$\Sigma(E) = \int_{C_{1'}} dp\, p^2 \frac{g^2(p)}{E - E_1(p) - E_2(p)} \tag{76}$$

$$= \int_{C_1} dp\, p^2 \frac{g^2(p)}{E - E_1(p) - E_2(p)}, \tag{77}$$

for E on the unphysical Riemann sheet defined by $\mathrm{Im}\, p_0 \leqslant 0$. To test this numerical procedure, let us consider the case that $\Sigma(E)$ defined by Eq. (72) can be calculated analytically. Such an analytic form can be obtained by taking the nonrelativistic kinematics $E_1(p) + E_2(p) = m_1 + m_2 + p^2/(2\mu)$ with $\mu = m_1 m_2/(m_1 + m_2)$ and a monopole form for the vertex function

$$g(p) = \frac{\lambda}{1 + p^2/\beta^2}, \tag{78}$$

where β is a cutoff parameter. The integration in $\Sigma(E)$ of Eq. (72) can then be done exactly to give the following simple form:

$$\Sigma(E) = \frac{\pi \mu \beta^3 \lambda^2}{2(p_0 + i\beta)^2}, \tag{79}$$

where p_0 is defined by $E = m_1 + m_2 + p_0^2/(2\mu)$. If the imaginary part of p_0 is positive (negative), it means that we choose the poles on the physical (unphysical) sheet. Only the pole with $\mathrm{Im}\, p_0 \leqslant 0$ on the unphysical sheet is called a resonance, as discussed in the previous section.

The resonance poles on the unphysical sheet ($\mathrm{Im}\, p_0 \leqslant 0$) obtained from using Eq. (79) to solve Eq. (75) are the solid curve displayed in Fig. 6 using the parameters $m_1 = m_N = 938.5$ MeV, $m_2 = m_\pi = 139.6$ MeV, and $M_0 = m_N + m_\pi + 600$ MeV and cutoff momentum $\beta =$ 800 MeV, for a range of coupling constant $0 \leqslant \lambda \leqslant 0.04$. We next solve Eqs. (75) and (77) by choosing contour C_1 illustrated in Fig. 5. The solutions are stable provided the path is not too close to the pole. The solutions completely agree with the solid curve of the exact solution and hence are not displayed in Fig. 6. Here we also note that Eq. (79) also allows us to calculate the poles by using the SP and TD methods. The results for λ values of 0.01, 0.02, 0.03, 0.04 are shown by the solid squares in Fig. 6. As expected, we confirm the previous findings that both SP and TD methods work well for the single-channel case.

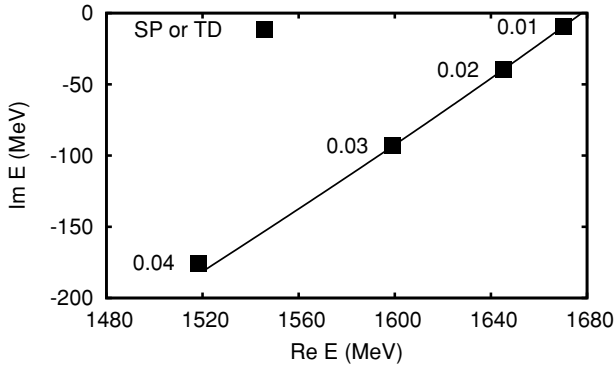

FIG. 6. λ dependence of the pole position of the one-channel, one-resonance model. The line represents the pole position of the t-matrix on the unphysical sheet. Solid squares are the pole positions extracted by using the SP and TD methods.

B. Two-channel, one-resonance case

The formula for the two-channel, one-resonance case can be easily obtained by extending the equations in the previous section to include channel label $i = 1, 2$. We thus have

$$t_{ij}(p', p; E) = v_{ij}(p', p; E) + \sum_k \int_{C_0} dq\, q^2 \frac{v_{ik}(p', q) t_{kj}(q, p; E)}{E - E_{k1}(q) - E_{k2}(q)}, \tag{80}$$

where $E_{kn}(p) = [m_{kn}^2 + p^2]^{1/2}$ with m_{kn} denoting the mass of the nth particle in channel k, and

$$v_{ij}(p', p; E) = g_i(p') \frac{1}{E - M_0} g_j(p). \tag{81}$$

Equations (80) and (81) lead to

$$t_{ij}(p', p; E) = \frac{g_i(p') g_j(p)}{E - M_0 - \Sigma_1(E) - \Sigma_2(E)}, \tag{82}$$

with

$$\Sigma_k(E) = \int_{C_0} dp\, p^2 \frac{g_k^2(p)}{E - E_{k1}(p) - E_{k2}(p)}. \tag{83}$$

For the physical scattering amplitude at a positive energy E, Eq. (80) is solved by setting $E \to E + i\epsilon$ with a positive $\epsilon \to 0$ and choosing C_0 along the real axis $0 \leqslant p \leqslant \infty$.

With Eq. (82), the poles of the scattering amplitudes are defined by

$$E - M_0 - \Sigma_1(E) - \Sigma_2(E) = 0. \tag{84}$$

The poles from solving the equation can be on one of the four Riemann sheets, pp, up, uu, and pu, as explained in Sec. III. The numerical procedure for finding the resonance poles on the uu-sheet is to solve Eq. (84) for $E = E_{11}(p_{01}) + E_{12}(p_{01}) = E_{21}(p_{02}) + E_{22}(p_{02})$ with $\mathrm{Im}\, p_{01} \leqslant 0$ and $\mathrm{Im}\, p_{02} \leqslant 0$. The integration path C_0 is changed to C_1 shown in Fig. 5(b) to calculate both self-energies $\Sigma_1(E)$ and $\Sigma_2(E)$ of Eq. (83). Of course the contour C_1 for the integration over the momentum for the ith channel must be below the pole p_{0i} defined by $E - E_{i1}(p_{0i}) - E_{i2}(p_{0i}) = 0$. Here we note that for finding the poles on the pu-sheet (up-sheet), the contour C_0 is replaced by C_1 only for $\Sigma_2(E)$ [$\Sigma_1(E)$].

To test numerical procedures and to further test the SP and TD methods, let us consider again the nonrelativistic kinematics $E_{i1}(p) + E_{i2}(p) = \Theta_i + p^2/(2\mu_i)$ with $\Theta_i = m_{i1} + m_{i2}$ and $\mu_i = m_{i1}m_{i2}/(m_{i1} + m_{i2})$. This will allow us to find the exact solutions by choosing the monopole form factor

$$g_i(p) = \frac{\lambda_i}{1 + p^2/\beta_i^2}. \tag{85}$$

We then have

$$\Sigma_i(E) = \frac{\pi \mu_i \beta_i^3 \lambda_i^2}{2(p_i + i\beta_i)^2}. \tag{86}$$

With Eq. (86), the poles defined by Eq. (84) can be found by solving algebraic equations. For numerical calculations, we consider a case similar to πN scattering in the S_{11} partial wave: (1) channel 1 is πN with $m_{11} = m_\pi = 139.6$ MeV, $m_{12} = m_N = 938.5$ MeV, and $\beta_1 = 800$ MeV, (2) channel 2 is ηN with $m_{21} = m_\eta = 547.45$ MeV, $m_{22} = m_N = 938.5$ MeV, and $\beta_2 = 800$ MeV, and (3) the bare mass is $M_0 = m_\pi + m_N + 600$ MeV. The results are shown in Fig. 7. The dash-dotted (solid) curves are the calculated poles on the uu-sheet (up-sheet) with the coupling constants $\lambda_1 = 0.02$ for $N_0 \to \pi N$ and a range of $\lambda_2 = 0$–0.02 for $N_0 \to \eta N$. We see that when λ_2 is 0, which is the single-channel case, the uu-pole and the up-pole are at the same position. They then split as λ_2 increases.

We next evaluate Eq. (83) for E on the uu-sheet, up-sheet, or pu-sheet by appropriately choosing the path C_0, as just described. The poles are found when the calculated $\Sigma_1(E)$ and $\Sigma_2(E)$ satisfy Eq. (84). We find that the poles obtained by this numerical procedure reproduce accurately the dash-dotted (uu-sheet), solid (up-sheet), and dashed (pu-sheet) curve in Fig. 7 and hence are omitted there. Thus this analytic continuation method can be used in practice to find the resonance poles (i.e., poles on the uu-sheet as defined in Sec. III) for the general case that $\Sigma_i(E)$ cannot be integrated analytically.

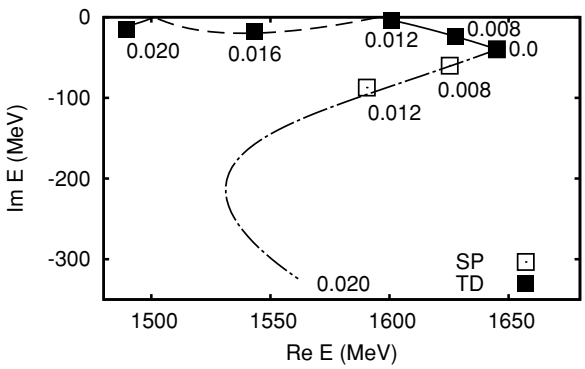

FIG. 7. λ_2 dependence of the pole positions on the uu-sheet (dash-dotted curve), up-sheet (solid curve), and pu-sheet (dashed curve) of the two-channel, one-resonance model. The open squares (solid squares) are obtained from using the SP (TD) method.

We now turn to examining the SP and TD methods. In Fig. 7, we show that the SP method (open squares) reproduces the poles (dash-dotted curve) on the uu-sheet only at $\lambda_2 \leqslant 0.015$. When λ_2 is larger than 0.015 where the magnitude of $\mathrm{Im}\, E_R$ continues to increase, the speed has no maximum and the SP method fails to find the pole. This is another example showing the limitation of the SP method. However, the TD method (solid squares) can reproduce the poles on the up-sheet (solid curve) and pu-sheet (dashed curve) in the considered range of parameters. Here we see that the SP and TD methods find different poles, which have different physical meanings in the Hamiltonian formulation. One can show [15] that the poles on the uu-sheet are due to the process that an unstable system is created and then decays during the collision and are called the resonance poles. The physical interpretations of the poles on the pu- and up-sheets remain to be developed.

It is interesting to point out here that the two-channel BW form analyzed in detail in the previous section can be derived from the two-channel, one-resonance model if the nonrelativistic kinematics is used. To see this, we first write the nonrelativistic relation between the S-matrix and the T-matrix:

$$S_{ij}(E) = \delta_{ij} + 2iT_{ij}(E), \tag{87}$$

$$T_{ij}(E) = -\pi\sqrt{\mu_i p_i \mu_j p_j}\, t_{ij}(p_i, p_j; E), \tag{88}$$

where p_i, the on-shell momentum in channel i is

$$p_i = \sqrt{2\mu_i(E - \Theta_i)}. \tag{89}$$

With this and the analytic form [Eq. (86)] for $\Sigma_i(E)$, we can write the $1 \to 1$ elastic scattering amplitude of Eq. (88) as

$$T_{11}(p_1, p_1, E) = \frac{-p_1\gamma_1(p_1)}{E - M(E) + ip_1\gamma_1(p_1) + ip_2\gamma_2(p_2)}, \tag{90}$$

where $\gamma_i(p_i) = \pi\mu_i g_i^2(p_i) > 0$ and

$$M(E) = M^0 + \sum_k P\int p^2 dp \frac{g_k^2(p)}{E - m_{k1} - m_{k2} - \frac{p^2}{2\mu_k}}, \tag{91}$$

where P means taking the principal-value integration. By using Eq. (87), we then have the $1 \to 1$ elastic part of the S-matrix:

$$S_{11} = \frac{E - M(E) - ip_1\gamma_1(p_1) + ip_2\gamma_2(p_2)}{E - M(E) + ip_1\gamma_1(p_1) + ip_2\gamma_2(p_2)}. \tag{92}$$

If the E dependence of $M(E)$ and $\gamma_i(p_i)$ are further neglected, Eqs. (90) and (92) are identical to what are usually called the two-channel BW resonant amplitude discussed in the previous section. Thus the conditions under which SP and TD methods are valid can be related now to the parameters of the vertex function $g_i(p)$ within this two-channel, one-resonance model.

C. Two-channel, two-resonance case

For the two-channel, two-resonance case, the scattering amplitude is defined by the same Eq. (80), but with the following driving term:

$$v_{ij}(p', p; E) = g_{i1}(p')\frac{1}{E - M_1}g_{j1}(p) + g_{i2}(p')\frac{1}{E - M_2}g_{j2}(p). \quad (93)$$

The scattering amplitude is then of the following form:

$$t_{ij}(p', p; E) = \sum_{\alpha,\beta} g_{i,\alpha}(p')[D^{-1}(E)]_{\alpha,\beta}g_{j,\beta}(p). \quad (94)$$

The propagator $D(E)$ in Eq. (94) is

$$[D(E)]_{\alpha,\beta} = [E - M_\alpha]\delta_{\alpha,\beta} - \Sigma_{\alpha,\beta}(E), \quad (95)$$

with

$$\Sigma_{\alpha,\beta}(E) = \sum_i \int_{C_0} dq\, q^2 \frac{g_{i,\alpha}(q)g_{i,\beta}(q)}{E - E_{i1}(q) - E_{i2}(q) + i\varepsilon}. \quad (96)$$

The poles are defined by

$$\begin{aligned}\mathrm{Det}D(E) &= [E - M_1 - \Sigma_{11}(E)][E - M_2 - \Sigma_{22}(E)] \\ &\quad - \Sigma_{12}(E)\Sigma_{21}(E) \\ &= 0. \end{aligned} \quad (97)$$

The numerical procedures of finding the resonance poles on the uu-sheet from Eqs. (96) and (97) are the same as that in the previous two sections. Namely, the path C_0 of Eq. (96) is set to be the path C_1 shown in Fig. 5 in evaluating the integrals for E on the uu-sheet where the on-shell momenta are $\mathrm{Im}p_i < 0$ for $i = 1, 2$ channels. To test this, we again choose the nonrelativistic kinematics and the monopole form factor like Eq. (85). The self-energy $\Sigma_{\alpha,\beta}(E)$ then takes the analytic form similar to Eq. (79). The condition of Eq. (97) can then be expressed in a analytic form from which the pole positions on the unphysical sheet can be easily obtained.

We only state that the resulting poles on the unphysical sheets are reproduced by the numerical this analytic continuation method just described. Instead, our focus here is to further test the SP and TD methods for the situation that two resonances are close and could overlap. We again consider πN and ηN channels and use the following form factor:

$$g_{i\alpha}(p) = \frac{\lambda_{i\alpha}}{1 + p^2/\beta_{i\alpha}^2}, \quad (98)$$

where $\alpha = 1, 2$ denote the αth bare state with mass M_α. The four cutoff parameters $\beta_{i\alpha}$ and four coupling constants $\lambda_{i\alpha}$ are taken to be $\beta_{11} = \beta_{12} = \beta_{21} = \beta_{22} = 800$ MeV, $\lambda_{11} = 0.005$, $\lambda_{12} = 0.01$, $\lambda_{21} = 0.003$, and $\lambda_{22} = 0.008$. One of the bare masses M_1 is fixed in the calculations. M_2 is defined by

$$M_2 = M_\pi + M_N + \tilde{M}_2, \quad (99)$$

where $\tilde{M}_2$ is varied for examining how the poles move as M_2 moves away from $M_1 = M_\pi + M_N + 550 = 1628$ MeV.

The pole positions are searched numerically by using the analytic continuation method just described. There are two poles on the uu-sheet and the other two are on the up-sheet. As $\tilde{M}_2$ varies, these two poles will develop two trajectories, as shown by the crosses connected by the solid curves shown in Fig. 8 for the uu-sheet and in Fig. 9 for the up-sheet. According to our findings in Sec. III, the poles $(M_R, -i\Gamma_R/2)$ found by the SP and TD methods should be compared with the poles on the uu- and up-sheets, respectively, of Figs. 8 and 9, respectively. We now discuss these two comparisons.

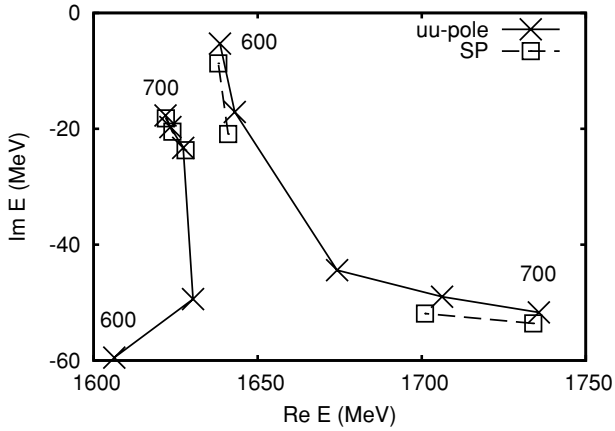

FIG. 8. Pole positions (crosses connected by solid lines) on the uu-sheet of the two-channel, two-resonance model. The results from using the SP method are the open squares connected by the dashed lines. The numbers on the figure are the value of $\tilde{M}_2$.

We see from Fig. 8 that, in the regions near $\tilde{M}_2 = 700$ MeV, the positions (ReE) of these two poles are far from each other and we find that the SP method (open squares connected by dashed lines near the point marked 700) works well. When $\tilde{M}_2$ is reduced to 600 MeV where the positions (ReE) of the two poles move closer, the SP method can find only one pole (open squares connected by dashed line) near the top end of the trajectory on the right-hand side. Apart from the points on the dashed lines, the SP method fails to find poles close to the poles on the solid curves, which are obtained numerically by the analytic continuation method.

The results for examining the TD case are shown in Fig. 9. We see that the TD method can find two poles on

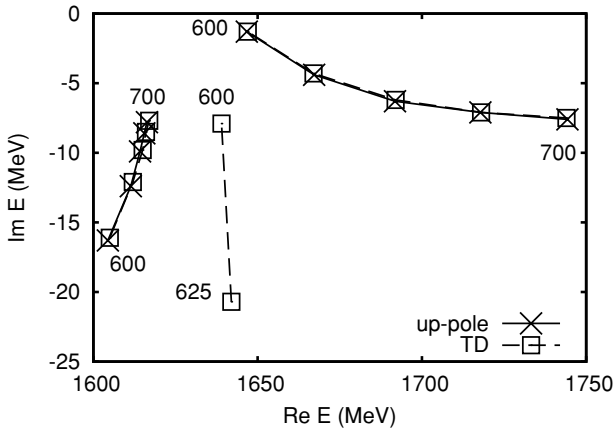

FIG. 9. Pole positions (crosses connected by solid lines) on the up-sheet of the two-channel, two-resonance model. The results from using the TD method are the open squares connected by the dashed lines. The numbers on the figure are the value of $\tilde{M}_2$.

the up-sheet in the considered range of $\tilde{M}_2 = 600$–700. The results are the open squares connected by dashed lines, which are indistinguishable from the crosses connected by solid curves, which were obtained by the analytic continuation method. But the TD method obtains another two poles at $\tilde{M}_2 = 600$ and $\tilde{M}_2 = 625$, as indicated by the dashed line in the middle of Fig. 9. The positions of these two poles are very close to those obtained from the SP method and they are interpreted as poles on the uu-sheet. As we have discussed in Sec. II, the TD method is sensitive to both the zero and the pole of the S-matrix on pp- and uu-sheets. In this example, the width of the poles on the uu-sheet becomes comparable to that of the poles on the up-sheet (zero on the physical sheet) and hence the TD method could find a pole on the uu-sheet. The results shown in Figs. 8 and 9 further indicate the limitation of SP and TD methods.

The results from these models have shown that the TD method based on Eq. (16), where the phase of the elastic channel is used instead of the eigenphases discussed in Refs. [23–25], gives both the resonance poles on the uu-sheet and the zeros (shadow poles). Our findings could provide some information for investigating the differences between Refs. [25] and [34]. We also want to mention here that an improved SP method using higher order derivatives of the amplitudes was proposed in Ref. [35]. It may be interesting to compare this method with the TD method. Although it could be interesting to address the questions concerning these recent developments, they are far from the main focus of this paper and will not be discussed further.

V. ANALYTIC CONTINUATION OF RESONANCE MODEL WITH UNSTABLE PARTICLE CHANNELS

For meson-baryon reactions, the nucleon resonances can decay into some unstable particle channels such as the $\pi\Delta$, ρN, and σN channels considered in the model of Ref. [9]. Here we discuss the analytic continuation method to find resonance poles within such a reaction model.

It is sufficient to consider the one-channel and one resonance case. The scattering formula is then identical to that presented in Sec. IV A. The only difference is that one of the particles in the open channel can further decay into a two-particle state. To be specific, let us consider the $\pi\Delta$ channel. Within the same Hamiltonian formulation [9] used in the previous section, the scattering amplitude can then be written as

$$t(p', p, E) = \frac{g_{N^*,\pi\Delta}(p')g_{N^*,\pi\Delta}(p)}{E - M_0 - \Sigma_{\pi\Delta}(E)}, \tag{100}$$

with

$$\Sigma_{\pi\Delta}(E) = \int_{C_2} p^2 dp \frac{g^2_{N^*,\pi\Delta}(p)}{E - E_\pi(p) - E_\Delta(p) - \Sigma_\Delta(p, E)}, \tag{101}$$

where

$$\Sigma_\Delta(p, E) = \int_{C_3} q^2 dq \frac{g^2_{\Delta,\pi N}(q)}{E - E_\pi(p) - [(E_\pi(q) + E_N(q))^2 + p^2]^{1/2}}. \tag{102}$$

To obtain the $\pi\Delta$ self-energy for complex E, the analytic structure of the integrand of Eq. (101) should be examined first. The discontinuity of the $\pi\Delta$ propagator in the integrand of Eq. (101) is the $\pi\pi N$ cut along the real axis between $\pm p_0(-p_0 \leqslant p \leqslant p_0)$, which is obtained by solving

$$E = E_\pi(p_0) + \left[(m_\pi + m_N)^2 + p_0^2\right]^{1/2}. \tag{103}$$

For finding the resonance poles on the uu-sheet with $\mathrm{Im}\, p_0 \leqslant 0$, the integration contour C_2 of Eq. (101) must be chosen below this cut, which is the dashed line in Fig. 10. There is also a singularity in the integrand of Eq. (101) at momentum $p = p_x$, which satisfies

$$E - E_\pi(p_x) - E_\Delta(p_x) - \Sigma_\Delta(p_x, E) = 0. \tag{104}$$

Physically, this singularity corresponds to the $\pi\Delta$ two-body scattering state. For E with large imaginary part, p_x can be below the $\pi\pi N$ cut, as also indicated in Fig. 10. Therefore the integration contour of momentum p must be chosen to be below the $\pi\pi N$ cut (dashed line) and the singularity p_x, such as the contour C_2 shown in Fig. 10.

The singularity position q_0 of the propagator in Eq. (102) depends on spectator momentum p as

$$E - E_\pi(p) = \{[E_\pi(q_0) + E_N(q_0)]^2 + p^2\}^{1/2}. \tag{105}$$

Therefore the singularity q_0 moves along the dashed curve in Fig. 11 when the momentum p varies along the path C_2 of Fig. 10. To analytically continue $\Sigma_\Delta(p, E)$ from positive energy E to the unphysical plane with $\mathrm{Im}\, p \leqslant 0$, we need to choose the contour C_3 of Eq. (102) that must be below q_0. A possible contour C_3 is the solid curve in Fig. 11.

To verify these numerical procedures described, we again consider nonrelativistic kinematics and the monopole form

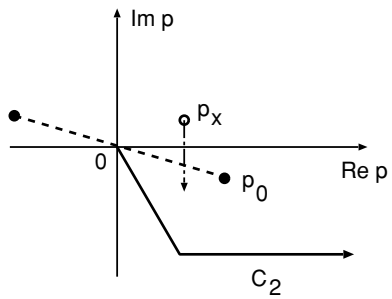

FIG. 10. Contour C_2 for calculating the $\pi\Delta$ self-energy on the unphysical sheet. See the text for explanations of the dashed line and the singularity p_x.

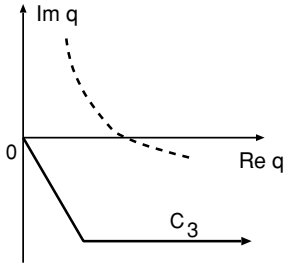

FIG. 11. Contour C_3 for calculating the πN self-energy on the unphysical sheet. The dashed curve is the singularity q_0 of the propagator in Eq. (102), which depends on the spectator momentum p on the contour C_2 of Fig. 10.

factor. With the similar analytic form of Eq. (79), we have

$$\Sigma_\Delta(p, E) = \frac{\pi \mu_{\pi N} g^2_{\Delta,\pi N} \beta^3_{\Delta,\pi N}}{2(\bar{k} + i\beta_{\Delta,\pi N})^2}, \tag{106}$$

where

$$\bar{k} = \left[2\mu_{\pi N}\left(E - 2m_\pi - m_N - \frac{p^2}{2\mu_{\pi\pi N}}\right)\right]^{1/2}, \tag{107}$$

with $\mu_{\pi\pi N} = m_\pi(m_\pi + m_N)/(2m_\pi + m_N)$. With Eq. (106), we can solve Eq. (104) and verify its relation with the $\pi\pi N$ cut as previously discussed and illustrated in Fig. 10. Equation (106) and the chosen monopole form factor also allow us to get

$$\Sigma_{\pi\Delta} = \int_{c_2} p^2 dp \frac{g^2_{N^*,\pi\Delta}}{(1 + p^2/\beta^2_{N^*,\pi\Delta})^2} \frac{1}{D_{\pi\Delta}(p, E)}, \tag{108}$$

with

$$D_{\pi\Delta}(p, E) = E - m_\pi - m_\Delta - \frac{p^2}{2\mu_{\pi\Delta}} - \frac{\pi \mu_{\pi N} g^2_{\Delta,\pi N} \beta^3_{\Delta,\pi N}}{2(\bar{k} + i\beta_{\Delta,\pi N})^2}. \tag{109}$$

Unfortunately, Eq. (108) cannot be integrated out analytically for directly checking our numerical procedure for searching resonance poles.

We test our analytic continuation method by the following procedure. We calculate Eq. (108) numerically to find the pole position E_R by solving $E_R - M_0 - \Sigma_{\pi\Delta}(E_R) = 0$ of the denominator of Eq. (100). With the parameters

$$\begin{aligned} \beta_{N^*,\pi\Delta} &= 800\ \text{MeV}, \quad g_{N^*,\pi\Delta} = 0.02\ \text{MeV}^{-1/2}, \\ \beta_{\Delta,\pi N} &= 200\ \text{MeV}, \quad g_{\Delta,\pi N} = 0.05\ \text{MeV}^{-1/2}, \\ M_0 &= 650\ \text{MeV} + m_\pi + m_N, \end{aligned}$$

we find $E_R = (1679.1, -33.6i)$ MeV. We then construct an approximate propagator

$$G^{\text{approx}}_{N^*}(E) = \frac{1}{E - E_R}. \tag{110}$$

For positive E, we find that $G^{\text{approx}}_{N^*}(E)$ is in good agreement with the direct calculation of $G_{N^*}(E) = 1/[E - M_0 - \Sigma_{\pi\Delta}(E)]$ by using Eq. (108). The results are shown in Fig. 12. It is clear that the resonance pole found by our analytic continuation method can reproduce what is expected for a resonance propagator for real positive E. In this way our numerical procedure is justified and can be applied to solve Eqs. (100)–(102).

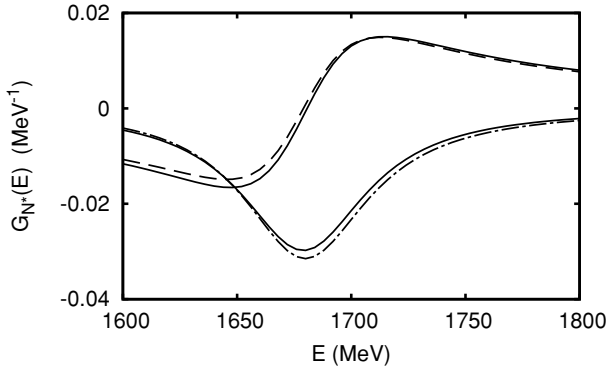

FIG. 12. N^* Green function. The solid (dash-dotted) curve is the real (imaginary) part of exact Green function $G_{N^*}(E) = 1/[E - M_0 - \Sigma_{\pi\Delta}(E)]$. They are compared with the dashed (dotted) curve of the real (imaginary) part of the approximate Green function $G^{\text{approx}}_{N^*}$.

VI. RESONANCE MODEL WITH NONRESONANT INTERACTIONS

With the numerical methods just described, we can proceed to extract the resonance poles within a coupled-channels model that also include nonresonant interactions. In this section, we explain how this can be done for the πN model developed in Refs. [9,22].

Recalling the formulations presented in Refs. [9,22], we have that the t-matrix considered is of the following form:

$$t_{ij}(p', p; W) = \bar{t}_{ij}(p', p; W) + \sum_{\alpha,\beta} \bar{\Gamma}_{i,\alpha}(p'; W)[D^{-1}(W)]_{\alpha,\beta}\bar{\Gamma}_{j,\beta}(p; W), \tag{111}$$

where i, j can be stable channels πN and ηN or unstable channels $\pi\Delta$, ρN, and σN and α denotes a bare resonant state with a mass M_α.

For extracting resonance poles, we now apply the methods presented in previous sections to choose appropriate contours for calculating various integrations on the unphysical E-plane with $\text{Im}\, p \leqslant 0$. The nonresonant t-matrix $\bar{t}_{ij}(p', p; E)$ is defined by the following coupled-channel equations with the nonresonant potential $v_{ij}(p', p)$:

$$\bar{t}_{ij}(p', p; E) = v_{ij}(p', p) + \sum_k \int_{C_4} dq\, q^2 \frac{v_{ik}(p', q)\bar{t}_{kj}(q, p; E)}{E - E_k(q) - \Sigma_k(q, E) + i\varepsilon}, \tag{112}$$

where the contour is $C_4 = C_1$ [Fig. 5(b)] for $k = \pi N, \eta N$ and $C_4 = C_2$ (Fig. 10) for $k = \pi\Delta, \rho N, \sigma N$, and

$$E_k(p) = \sqrt{m^2_{k1} + p^2} + \sqrt{m^2_{k2} + p^2}. \tag{113}$$

TABLE I. Resonance poles extracted from the πN scattering amplitudes of Ref. [22].

	Analytic continuation		Speed plot		Time delay		PDG	
	Re	Im	Re	Im	Re	Im	Re	Im
S11	1540	−191	–	–	1543	−52	1490–1530	−45–125
	1642	−41	1644	−89	1645	−61	1640–1670	−75–90
S31	1563	−95	1574	−67	1616	−53	1590–1610	−57–60
P33	1211	−50	1212	−49	1212	−49	1209–1211	−49–51
D13	1521	−58	1525	−57	1522	−11	1505–1515	−52–60
F15	1674	−53	1671	−59	1683	−24	1665–1680	−55–68

The self-energies in Eq. (112) are $\Sigma_{\pi N}(q, E) = \Sigma_{\eta N}(q, E) = 0$, and $\Sigma_{\pi\Delta}(q, E)$, $\Sigma_{\rho N}(p, E)$, and $\Sigma_{\sigma N}(q, E)$ are defined by the same Eq. (101) with appropriate changes of mass parameters and the choice of contour C_2 and C_3 shown in Figs. 10 and 11.

The dressed vertex $\bar{\Gamma}_i(p; W)$ is determined by the bare vertex $\Gamma_i(p)$ and the meson-baryon loop,

$$\bar{\Gamma}_{i,\alpha}(p; E) = \Gamma_{i,\alpha}(p) + \sum_k \int_{C4} dq\, q^2 \frac{\bar{t}_{ik}(p, q; E)\Gamma_k(q; E)}{E - E_k(q) - \Sigma_k(p, E) + i\varepsilon}. \tag{114}$$

The resonance propagator $D(E)$ in Eq. (111) is

$$[D(E)]_{\alpha,\beta} = [E - M_\alpha]\delta_{\alpha,\beta} - \Sigma_{\alpha,\beta}(E), \tag{115}$$

with

$$\Sigma_{\alpha,\beta}(E) = \sum_k \int_{C_4} dq\, q^2 \frac{\Gamma_{k,\alpha}(q)\bar{\Gamma}_{k,\beta}(q; E)}{E - E_k(q) - \Sigma_k(q, E) + i\varepsilon}. \tag{116}$$

In Ref. [22], these equations are solved on the real axis by using the standard method of subtraction. Here we solve the equations by choosing the contours as indicated earlier. We first verify that our numerical results obtained here for positive real E agree with that of Ref. [22]. This establishes our numerical procedure in this complex five-channel model.

Here we show the results for some of the S, P, D, and F partial waves of πN scattering within the model of Ref. [22]. We search the resonance poles by looking for zeros of the resonant propagator $D(E)$ defined by Eq. (115). Our results from using the analytic continuation method are shown in the second column of Table I. They are compared with those extracted by using the SP and TD methods described in the previous sections as well as the values listed by the PDG. The BW resonance parameters are also given by the PDG, but these are not considered here. We see in Table I that the SP method fails to find the first resonance pole in the S_{11} partial wave. We also see that although the real parts of the resonance poles from different approaches are within the ranges of those reported by the PDG, the extracted imaginary parts can differ by as much as a factor of 2 or 3.

The model of Ref. [22] is currently being improved by also fitting other data of πN and γN reactions. For example, some progress has been made to also fit the data of $\pi N \to \pi\pi N$ [36], $\gamma N \to \pi N$ [37], and $\pi N \to \eta N$ [38]. We thus do not include the results for other partial waves in Table I. Our purpose here is to simply demonstrate how the analytic continuation method works for a realistic model. The full resonance parameters, including the extracted residues and the relations to the BW parameters listed by the PDG, extracted from our complete analysis of all $\pi N\gamma$, $N \to \pi N, \eta N, \pi\pi N$ reactions will be reported elsewhere.

We now turn to a discussion of whether the extracted resonance pole M can be used to evaluate the N^* propagator defined by Eq. (115) for the physical positive E. Let us consider the S_{31} case listed in Table I. Its N^* propagator $G_{N^*}(E)$ can be written as

$$G_{N^*}(E) = \frac{1}{E - M_0 - \Sigma(E)}, \tag{117}$$

$$\Sigma(E) = \Sigma_{\pi N}(E) + \Sigma_{\pi\Delta}(E) + \Sigma_{\rho N}(E). \tag{118}$$

By using the analytic continuation methods described in the previous sections, the resonance energy $M = (1563 - i95)$ MeV is found numerically by solving

$$M - M_0 - \Sigma(M) = 0. \tag{119}$$

We now perform the Laurent expansion of $G_{N^*}(E)$ for real E around the pole position M and obtain

$$\begin{aligned} G_{N^*}(E) &= \left[(1 - \Sigma'(M))(E - M) - \frac{1}{2}\Sigma''(M)(E - M)^2 + \cdots\right]^{-1} \\ &= \frac{1}{E - M}\left[\frac{1}{1 - \Sigma'(M) - \frac{1}{2}\Sigma''(M)(E - M) + \cdots}\right] \\ &= \frac{1}{E - M}\left[\frac{1}{1 - \Sigma'(M)} + \frac{\Sigma''(M)(E - M)}{2(1 - \Sigma'(E))^2} + \cdots\right] \\ &= \frac{1}{E - M} \cdot \frac{1}{1 - \Sigma'(M)} + \frac{\Sigma''(M)}{2(1 - \Sigma'(M))^2} + \cdots. \end{aligned} \tag{120}$$

The naive $1/(E - M)$ works well for a model studied in the previous section. However, when the enery dependence of the self-energy Σ becomes large, two important modifications should be considered: (1) At the pole, the residue is not one but modified by the field renormalization factor $Z = 1/(1 - \Sigma'(M))$. (2) The second term of the last expression gives a constant term.

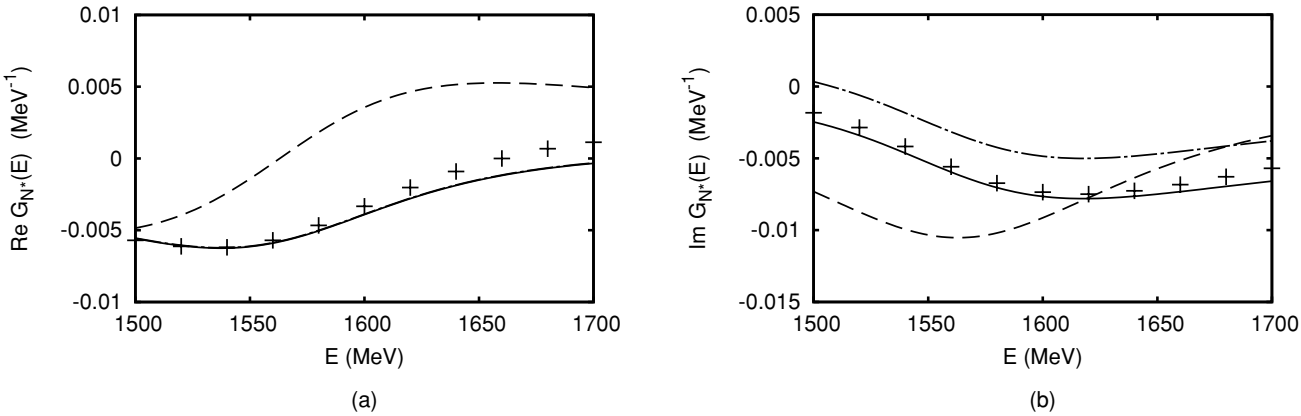

FIG. 13. Comparisons of various resonance propagators: exact propagator $G_{N^*}(E)$ (crosses), $G^{(0)}_{N^*}(E)$ (dashed curve), $G^{(1)}_{N^*}(E)$ (dash-dotted curve), and $G^{(2)}_{N^*}(E)$ (solid curve). The real and imaginary parts are shown in panels (a) and (b), respectively.

With the expansion of Eq. (120), we can introduce three different approximate forms for the N^* propagator:

$$G^{(0)}_{N^*}(E) = \frac{1}{E - M}, \tag{121}$$

$$G^{(1)}_{N^*}(E) = \frac{1}{E - M} \cdot \frac{1}{1 - \Sigma'(M)}, \tag{122}$$

$$G^{(2)}_{N^*}(E) = \frac{1}{E - M} \cdot \frac{1}{1 - \Sigma'(M)} + \frac{\Sigma''(M)}{2[1 - \Sigma'(M)]^2}. \tag{123}$$

In Fig. 13, we compare these three approximate propagators with the exact result of $G_{N^*}(E)$ of Eq. (117). The simple $G^{(0)}_{N^*}(E)$ (dashed curves) of Eq. (121) are far from the exact Green function $G_{N^*}(E)$ (cross) defined by Eq. (117). When the factor $1/[1 - \Sigma'(M)]$ is included, we obtain the dashed-dotted curves for $G^{(1)}_{N^*}(E)$. The solid curves are from $G^{(2)}_{N^*}(E)$. We see that the constant term $\frac{\Sigma''(M)}{2[1-\Sigma'(M)]^2}$ of Eq. (123) mainly affects the imaginary part of the propagator.

Equation (120) shows that the simple pole approximation $G^{(0)}_{N^*}(E) = \frac{1}{E-M}$, which can be cast into the usual BW form $1/(E - M_R + i\Gamma_R/2)$ with $M_R = \mathrm{Re}M$ and $\Gamma_R = -2\,\mathrm{Im}M$, works poorly. We also find that the pole parametrizations of the resonant propagator using the poles extracted by the TD and SP methods also work poorly. For the considered S_{31} case, the pole positions from using these two methods are $E_{\mathrm{SP}} = (1574, -67i)$ and $E_{\mathrm{TD}} = (1616, -53i)$, as given in Table I. In Fig. 14, we compare the exact propagator (crosses) $G_{N^*}(E)$ of Eq. (117) with the following two propagators:

$$G_{N^*,\mathrm{SP}}(E) = \frac{1}{E - E_{\mathrm{SP}}}, \tag{124}$$

$$G_{N^*,\mathrm{TD}}(E) = \frac{1}{E - E_{\mathrm{TD}}}. \tag{125}$$

Clearly, phenomenological forms Eqs. (124) and (125) cannot account for the complex coupled-channel resonant mechanisms.

VII. SUMMARY

In this paper, we have presented a pedagogical study of the commonly used speed-plot and time-delay methods for extracting the resonance parameters from the empirically determined partial-wave amplitudes. Using a two-channel Breit-Wigner form of the S-matrix, we show that the poles extracted by using theses two methods are on different Riemann sheets. The SP method can find resonance poles on

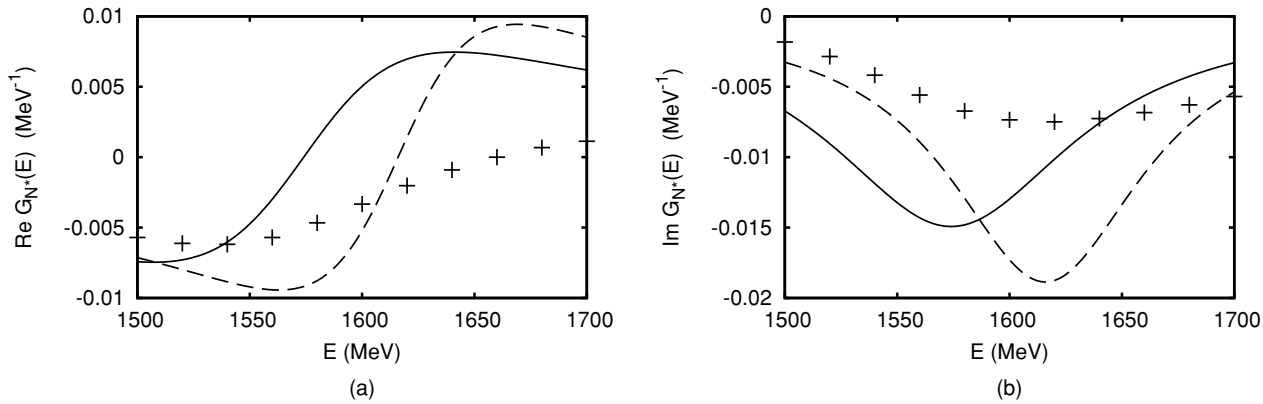

FIG. 14. The resonant propagator $G_{N^*}(E)$ (crosses) compared with $G_{N^*,\mathrm{SP}}(E)$ (solid curve) using the SP poles and $G_{N^*,\mathrm{TD}}(E)$ (dashed curve) using the TD poles. The real and imaginary parts are shown in panels (a) and (b), respectively.

the unphysical uu-sheet, whereas the TD method can find poles and zeros of the S-matrix on uu- or pp-sheets and therefore its validity is sensitive to the poles on the up- or pu-sheets. Furthermore, we also show numerically that these two methods can fail to find those poles. Our results support the previous findings that these two methods must be used with caution in searching for nucleon resonances from the meson-nucleon reaction data in the region where coupled-channel effects are important.

We then develop an analytic continuation method for extracting the resonance poles within a Hamiltonian formulation of meson-nucleon reactions. The main focus is on resolving the complications from the coupling with the unstable $\pi\Delta$, ρN, and σN channels that can decay into $\pi\pi N$ states. Explicit numerical procedures are presented and verified within several exactly solvable models. The results from these models are also used to further demonstrate the limitation of the SP and TD methods.

As a first application of the developed analytic continuation method, we present the results from analyzing the S_{11}, S_{31}, P_{33}, D_{13}, and F_{15} amplitudes of the dynamical coupled-channels model of πN reactions developed in Ref. [22]. We also analyze the resonance propagators and show that the simple pole parametrization of the resonant propagator using the poles extracted from SP and TD methods works poorly.

With the progress made in this work, we can proceed to extract all nucleon resonance parameters within the model of Ref. [22]. However, this can be done more accurately only when the coupling with the unstable $\pi\Delta$, ρN, and σN channels are better determined by also fitting the two-pion production data. Our progress in this direction will be reported elsewhere.

ACKNOWLEDGMENTS

This work is supported by the Japan Society for the Promotion of Science, Grant-in-Aid for Scientific Research(C) 20540270, and by the US Department of Energy, Office of Nuclear Physics Division, under Contract No. DE-AC02-06CH11357 and Contract No. DE-AC05-060R23177, under which Jefferson Science Associates operates Jefferson Lab.

[1] W.-T. Chiang and F. Tabakin, Phys. Rev. C **55**, 2054 (1997).
[2] H. Feshbach, *Theoretical Nuclear Physics: Nuclear Reactions* (John Wiley & Sons, Inc., 1992).
[3] G. Hoehler and A. Schulte, πN Newsletter **7**, 94 (1992).
[4] G. Hoehler, πN Newsletter **9**, 1 (1993).
[5] L. Eisenbud, Ph.D. dissertation, Princeton University, 1948 (unpublished).
[6] E. P. Wigner, Phys. Rev. **98**, 145 (1955).
[7] V. D. Burkert and T.-S. H. Lee, Int. J. Mod. Phys. E **13**, 1035 (2004).
[8] W.-M. Yao *et al.* (Particle Data Group), J. Phys. G **33**, 1 (2006), http://pdg.lbl.gov.
[9] A. Matsuyama, T. Sato, and T.-S. H. Lee, Phys. Rep. **439**, 193 (2007).
[10] R. G. Newton, J. Math. Phys. **1**, 319 (1960).
[11] R. G. Newton, J. Math. Phys. **2**, 188 (1961).
[12] R. E. Peierls, Proc. R. Soc. London A **253**, 16 (1959).
[13] K. J. Le Couteur, Proc. R. Soc. London A **256**, 115 (1960).
[14] M. Kato, Ann. Phys. (NY) **31**, 130 (1965).
[15] M. L. Goldberger and K. M. Watson, *Collision Theory* (Robert E. Krieger Publishing Company, Inc., 1975).
[16] R. H. Dalitz and R. G. Moorhouse, Proc. R. Soc. London A **318**, 279 (1970).
[17] H. M. Nussenzveig, Phys. Rev. D **6**, 1534 (1972).
[18] F. T. Smith, Phys. Rev. **118**, 349 (1960).
[19] N. G. Kelkar, M. Nowakowski, and K. P. Khemchandani, Nucl. Phys. **A724**, 357 (2003).
[20] N. G. Kelkar, M. Nowakowski, K. P. Khemchandani, and S. R. Jain, Nucl. Phys. **A730**, 121 (2004).
[21] N. G. Kelkar, M. Nawakowski, and K. P. Khemchandani, J. Phys. G **29**, 1001 (2003).
[22] B. Juliá-Díaz, T.-S. H. Lee, A. Matsuyama, and T. Sato, Phys. Rev. C **76**, 065201 (2007).
[23] A. U. Hazi, Phys. Rev. A **19**, 920 (1979).
[24] A. Igarashi and I. Shimamura, Phys. Rev. A **70**, 012706 (2004).
[25] H. Haberzettl and R. Workman, Phys. Rev. C **76**, 058201 (2007).
[26] Y. Fujii and M. Kato, Phys. Rev. **188**, 2319 (1969).
[27] Y. Fujii and M. Fukugita, Nucl. Phys. **B85**, 179 (1975).
[28] A. M. Badalyan, L. P. Kok, M. I. Polikarpov, and Yu. A. Simonov, Phys. Rep. **82**, 31 (1982).
[29] R. J. Eden and J. R. Taylor, Phys. Rev. **133**, B1575 (1964).
[30] R. G. Newton, *Scattering Theory of Waves and Particles* (Springer-Verlag, New York, 1982).
[31] Yu. V. Orlov and V. V. Turovtsev, Sov. Phys. JETP **59**, 902 (1989).
[32] B. C. Pearce and I. R. Afnan, Phys. Rev. C **30**, 2022 (1984).
[33] B. C. Pearce and B. F. Gibson, Phys. Rev. C **40**, 902 (1989).
[34] N. G. Kelkar and M. Nowakowski, Phys. Rev. A **78**, 012709 (2008).
[35] S. Ceci, J. Stahov, A. Svarc, S. Watson, and B. Zauner, Phys. Rev. D **77**, 116007 (2008).
[36] H. Kamano, B. Juliá-Díaz, T.-S. H. Lee, A. Matsuyama, and T. Sato, Phys. Rev. C **79**, 025206 (2009).
[37] B. Juliá-Díaz, T.-S. H. Lee, A. Matsuyama, T. Sato, and L. C. Smith, Phys. Rev. C **77**, 045205 (2008).
[38] J. Durand, B. Juliá-Díaz, T.-S. H. Lee, B. Saghai, and T. Sato, Phys. Rev. C **78**, 025204 (2008).